Fingerprint ridges allow primates to regulate grip

Seoung-Mok Yum[a,1], In-Keun Baek[a,1,2], Dongpyo Hong[a], Juhan Kim[a], Kyunghoon Jung[a], Seontae Kim[a], Kihoon Eom[a], Jeongmin Jang[a], Seonmyeong Kim[a], Matlabjon Sattorov[a,b,c], Min-Geol Lee[d], Sungwan Kim[e], Michael J. Adams[f,3], and Gun-Sik Park[a,b,c,g,3]

[a]Center for THz-Driven Biomedical Systems, Department of Physics and Astronomy, College of Natural Sciences, Seoul National University, Seoul 08826, Republic of Korea; [b]Center for Applied Electromagnetic Research, Advanced Institute of Convergence Technology, Suwon 16229, Republic of Korea; [c]R&D Department, Seoul-Teracom, Inc., Suwon 16229, Republic of Korea; [d]Cutaneous Biology Research Institute, Department of Dermatology, College of Medicine, Yonsei University, Seoul 03722, Republic of Korea; [e]Department of Biomedical Engineering, College of Medicine, Seoul National University, Seoul 03080, Republic of Korea; [f]School of Chemical Engineering, University of Birmingham, Birmingham GL51 9RE, United Kingdom; and [g]Institute of Applied Physics, Seoul National University, Seoul 08826, Republic of Korea

Edited by J. Edward Colgate, Northwestern University, Evanston, IL, and accepted by Editorial Board Member John A. Rogers October 8, 2020 (received for review June 4, 2020)

Fingerprints are unique to primates and koalas but what advantages do these features of our hands and feet provide us compared with the smooth pads of carnivorans, e.g., feline or ursine species? It has been argued that the epidermal ridges on finger pads decrease friction when in contact with smooth surfaces, promote interlocking with rough surfaces, channel excess water, prevent blistering, and enhance tactile sensitivity. Here, we found that they were at the origin of a moisture-regulating mechanism, which ensures an optimal hydration of the keratin layer of the skin for maximizing the friction and reducing the probability of catastrophic slip due to the hydrodynamic formation of a fluid layer. When in contact with impermeable surfaces, the occlusion of the sweat from the pores in the ridges promotes plasticization of the skin, dramatically increasing friction. Occlusion and external moisture could cause an excess of water that would defeat the natural hydration balance. However, we have demonstrated using femtosecond laser-based polarization-tunable terahertz wave spectroscopic imaging and infrared optical coherence tomography that the moisture regulation may be explained by a combination of a microfluidic capillary evaporation mechanism and a sweat pore blocking mechanism. This results in maintaining an optimal amount of moisture in the furrows that maximizes the friction irrespective of whether a finger pad is initially wet or dry. Thus, abundant low-flow sweat glands and epidermal furrows have provided primates with the evolutionary advantage in dry and wet conditions of manipulative and locomotive abilities not available to other animals.

epidermal ridge function | finger pad friction | moisture regulation | capillary evaporation

There is a resurgence of interest in the friction of the human finger pads, particularly for smooth surfaces, following the advent of touchscreens with haptic feedback (1) and artificial hands for robotic and prosthetic applications (2), but the long-standing question of the role the fingerprint ridges in grip events, which critically depends on the friction, is not fully resolved. Grip is central for many of our and other primate activities, e.g., the use of sports equipment, climbing trees for foraging purposes, and the precision manipulation of objects such as eating fruit. It is believed that the fingerprint ridges on the volar regions of the hands and feet play a crucial role in improving grip by allowing interlocking with contacting surfaces (3, 4) provided that they are sufficiently rough (5–8). Consequently, they are commonly referred to as friction ridges (9). Sweating improves grip as demonstrated, for example, by measuring the sliding resistance of the footpads of rats, tenrecs, rock hyrax, and rabbits after running on a treadmill (10). For smooth surfaces, it has been suggested that the ridges reduce the friction by depleting the contact area (11) since the friction of skin is described by the adhesion mechanism (12) as the product of interfacial shear stress required to rupture intermolecular interactions, such as van der Waals, and the contact area over which these bonds act. However, as a result of an increase in the contact area, the friction of human finger pads, for example, is increased substantially by moisture plasticization that softens the fingerprint ridges, either through the occlusion of moisture secreted from the eccrine sweat glands when in contact with an impermeable surface or by wetting from an external source (5, 12). Unlike the other regions of the skin, the sweat glands beneath the ridges respond to emotional states and anxiety, rather than primarily for thermoregulation purposes (13), which is thus a "fight or flight" response (10). Moreover, the volar regions of human hands and feet have a high density of sweat glands ($>300\ \mathrm{cm}^{-2}$) and possess 25% of the total number although occupying only about 5% of the total skin area (13). The sweat pores are readily visualized by grasping a glass with wet finger pads (Fig 1 *A*–*C*). The helical geometry of the associated sweat ducts may be imaged by optical coherence tomography (Fig. 1*D*). Fig 1 *D* and *F* also shows how the epidermal ridges in the fully occluded state are flattened when compressed against a glass plate.

The hydration of fully occluded fingerprint skin due to perspiration does not exceed a certain value while gripping (12, 14).

Significance

Why have primates evolved epidermal ridges on the volar regions of the hands and feet and with a much greater density of sweat glands than flat skin, which respond to anxiety rather than act as a thermoregulation mechanism? During contact with solid objects, the ridges are important for grip and precision manipulation by regulating moisture levels from either external sources or the sweat pores so that the friction is maximized and catastrophic slip is inhibited. An understanding of the underlying mechanisms involved has become particularly important with the almost ubiquitous contact of the finger pads with flat screens and recent developments in haptic feedback using ultrasonic vibrations for which the performance is critically related to the friction.

Author contributions: I.-K.B., D.H., M.J.A., and G.-S.P. designed research; S.-M.Y., I.-K.B., J.K., K.J., Seontae Kim, K.E., J.J., Seonmyeong Kim, M.S., M.J.A., and G.-S.P. performed research; S.-M.Y., I.-K.B., and D.H. contributed new reagents/analytic tools; S.-M.Y., I.-K.B., J.K., K.J., M.-G.L., Sungwan Kim, and G.-S.P. analyzed data; and S.-M.Y., I.-K.B., M.J.A., and G.-S.P. wrote the paper.

The authors declare no competing interest.

This article is a PNAS Direct Submission. J.E.C. is a guest editor invited by the Editorial Board.

[1]S.M.Y. and I.K.B. contributed equally to this work.

[2]Present address: Mechatronics R&D Center, Samsung Electronics Co., Ltd., Hwasung 18448, Republic of Korea.

[3]To whom correspondence may be addressed. Email: gunsik@snu.ac.kr or m.j.adams@bham.ac.uk.

This article contains supporting information online at https://www.pnas.org/lookup/suppl/doi:10.1073/pnas.2001055117/-/DCSupplemental.

First published November 30, 2020.

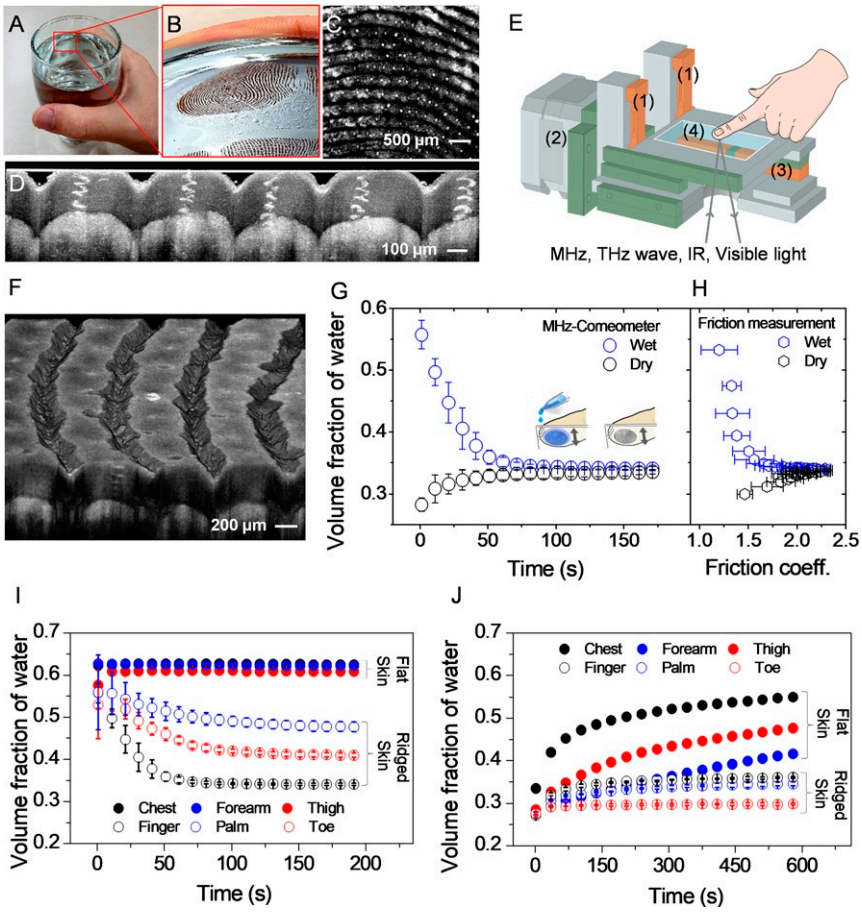

Fig. 1. (*A–C*) Optical images of a finger pad compressed against smooth glass. (*D*) IR-OCT image of a fingerprint showing helical sweat ducts. (*E*) Schematic diagram of the equipment for measuring the friction and imaging the moisture in the furrows, which shows the (*1*) tangential transducers, (*2*) stepper motor for driving translation stage, (*3*) normal transducer, and (*4*) glass plate. (*F*) IR-OCT image of the epidermal ridges and furrows in the fully occluded state compressed against smooth glass. (*G*) The hydration kinetics as measured using a MHz-Corneometer for an initially "wet" and "dry" finger pad; regardless of the initial wet or dry conditions, the volume fraction of the moisture converges to an asymptotic value. (*H*) Relationship between frictional force and the hydration level showing that the maximum friction is achieved at the converged hydration state. (*I* and *J*) Hydration levels of ridged and unridged skin in contact with glass as measured using a Corneometer when initially in the wet (*I*) and dry (*J*) states.

Moreover, André et al. (15) reported that the hydration of a finger pad tends toward a value that maximizes the friction during a gripping task. A number of reviews on the friction and lubrication of human skin have been published (12, 16–20), which indicate that there is an as-yet unknown moisture regulation mechanism for optimizing the grip of ridged skin. For contacts with glass, we have applied measurement techniques based on electromagnetic waves with frequencies in the megahertz (MHz), terahertz (THz), infrared (IR), and visible ranges to characterize and image the temporal evolution of moisture in the furrows arising from occlusion and external wetting. It is shown that the capillary evaporation of external moisture is initially enhanced by the epidermal furrows behaving as a microfluidic array with sharp corners but which allows a level of moisture to be retained that optimizes grip. The plasticization of the ridges leads to an intimate contact with a surface that prevents excess moisture due to the blocking of the sweat pores, which is the mechanism by which the secretion of sweat is limited in an occluded contact.

Results

The measurements (*Materials and Methods*) involved contacting finger pads with glass using the equipment shown schematically in Fig. 1*E* (*SI Appendix*, Fig. S1 *A* and *B*); hydrophilic glass was used unless stated that it is hydrophobic. The subjects were males aged 27 to 33 years. The initial moisture conditions were dry and wet, for which in the latter case a small droplet of water was imposed between the finger pad and glass. A normal force of 0.48 ± 0.04 N was maintained for the measurements of the friction (*SI Appendix*, Fig. S1*C* and *Materials and Methods*) and also those based on a Corneometer moisture sensor where a megahertz surface wave penetrates to a depth of 20 μm (*SI Appendix*, Fig. S2), terahertz time-domain spectroscopy (THz-TDS) (*SI Appendix*, Fig. S3), infrared optical coherence tomography (IR-OCT), and optical microscopy.

Fig 1 *G* and *H* demonstrates that the moisture arising from occlusion and external wetting tends to a path-independent steady-state volume fraction (*SI Appendix*, Fig. S4) that corresponds to the maximum value of the friction, thus ensuring optimal grip; the data were measured using a MHz-Corneometer. A similar tendency was shown for another participant with a little different converging time as shown in Fig. S5 *A* and *B*. In addition, the temporal evolution to a steady-state hydration for other participants is shown in *SI Appendix*, Fig. S5*C*.

Moreover, it appears that there is an approximate trend for the friction to increase from the little finger to the thumb (*SI Appendix*, Fig. S8), which would correspond to an increase in the contact area. For the wet case, the hydration level decreases linearly up to about 40 s followed by a slower rate and reaching a steady state at ∼70 s. However, for the dry case, the hydration level increases at a decreasing rate and reaches a steady state

after approximately the same time period as the wet case. Fig. 1*I* shows that such evaporation behavior in the wet state can only be observed with ridged but not flat skin, e.g., the chest, forearm, or thigh. In addition, for initially dry flat skin, Fig. 1*J* illustrates that the volume fraction of moisture does not tend to a steady-state value unlike occluded ridged skin; i.e., it does not exhibit homeostasis even though it has furrows but of much smaller number density and size (21). The temporal increase in the volume fraction of moisture in the occluded state is much greater for the flat compared with the ridge skin, which partly reflects the much greater sweat secretion rate of flat skin (13).

Data for the wet case are presented in Fig. 2. The optical images (Fig. 2 *A* and *B*) show that there is an initially saturated region due to the insertion of a water droplet but gradually the furrows lose the water as shown by the light regions between the contacting ridges. This drying phenomenon is quantified more clearly in Fig. 2*D*. These moisture profiles are calculated from the IR-OCT cross-sectional images of a furrow at different time intervals (Fig. 2*C*) with the location of the three-phase contact lines corresponding to the loss of scattering at the air–glass interface. The distribution of water was calculated from the change in the apparent geometry of the furrow. The depth of moisture in a furrow at a particular location, h_{water}, was estimated using the equation

$$h_{water} = (l - l_{dry})/(n_{water} - n_{air}), \quad [1]$$

where l and l_{dry} are the distances between the glass and skin on the OCT image in the current and initially dry states, and n_{water} and n_{air} are the refractive indexes of water and air. We sectionized the furrows of Fig. 2*C* into 25 regions and calculated the distribution of water to construct the cross-sectional images of Fig. 2*D*. Here in Fig. 2*D*, the curvature of the side meniscus is determined by the hydrophobic ridge and hydrophilic glass. It can be clearly confirmed by the visualized images in *SI Appendix*, Fig. S6. In Fig. 2*D*, at 20 s, side menisci are observed at the corners between the glass and the summits of the ridges as the bulk meniscus recedes due to evaporation, which at 60 s causes the side menisci to disappear. The reduction in the mean maximum heights of the moisture in the furrows due to the evaporation was measured by both the IR-OCT and THz-TDS (Fig. 2*E*). Fig. 2*F* exemplifies the variability of the IR-OCT data for the mean depth of the furrows at the center of individual furrows as a function of time; the change in depth reflects that of the moisture caused by the difference in refractive index of water and air. There is a corresponding variability in the fill lengths of moisture in the furrows (Fig. 2*G*). The near constant evaporation rate up to approximately 40 s arises primarily from the receding bulk menisci and corresponds to the linear reduction in the volume fraction of water in the finger pad up to this time period (Fig. 1*G*). Much slower evaporation from the side menisci is observed after 40 s as the steady-state hydration level is approached with the disappearance of the side meniscus after 30 s (Fig. 2*D*). The

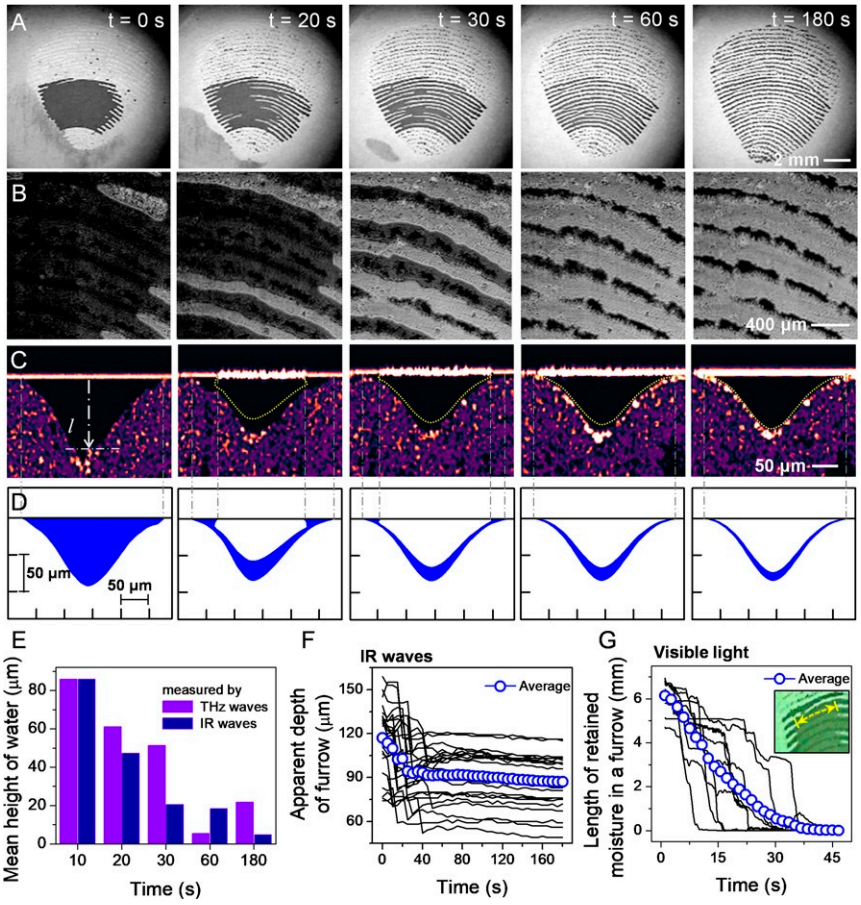

Fig. 2. The drying of moisture in furrows due to evaporation for an initially wet finger pad in contact with glass as a function of time. (*A*) Optical images. (*B*) Enlarged regions of *A*. (*C*) IR-OCT cross-sectional images of a typical furrow where the dashed yellow lines delineate the meniscus and *l* is the depth of the furrows. (*D*) Cross-sectional images of the moisture calculated from *C*. (*E*) Corresponding mean maximum depths of the moisture as a function of time as measured by THz-TDS and IR-OCT. (*F*) Apparent depth at the center of individual furrows as a function of time as measured in IR-OCT images. The changes in the apparent mean depths reflect a fast evaporation rate during the initial period of 40 s after which the rate is much slower. (*G*) Fill length of moisture in individual furrows as a function of time.

formation of bulk and side menisci is also observed by the IR-OCT tomographical snapshot images of a wet finger pad after the evaporation has initiated (Fig 3 *A*–*C*). In Fig. 3 *D*–*G*, the yellow dashed lines are interfaces of the water and air. These not fully scaled lines are drawn to make the observation more clear, which shows the shapes of side meniscus in Fig. 3*F* and bulk meniscus in Fig. 3*G* and how the evaporation starts in Fig. 3*E*. When there is no water just below the glass, the IR wave is scattered more on the glass surface. Distortions of the furrow are clearly observed in the images of Fig. 3 *E*–*G* at the interface of air and water. The curvatures of yellow dashed lines are not fully scaled. In Fig. 3*E*, considering that there is no scattered IR wave on the glass and the apparent height of furrow center, the yellow dashed line is drawn. The yellow dashed line in Fig. 3*F* is described in Fig. 2. In Fig. 3*G*, the variation of the furrow height along the length of the valley is observed with a slow change at the interface of air and water. The resulting curvature of the interface also depends on the hydrophilicity of the glass. Here we observe some variation of furrow height along the valley of the height. The evaporated moisture from the menisci is clearly observed by using IR-OCT (Fig 4 *A* and *B*) and a visible light-charge coupled device (CCD) camera (Fig. 4*C*). Both hydrophobic (Fig. 4*A*) and hydrophilic (Fig. 4*B*) glass (*Materials and Methods*) are used to observe the cross-sections of evaporating menisci using IR-OCT by a dispersion of fluorescent nanoparticles. The visibility of condensed water drops on the glass from evaporated moisture is much improved with hydrophobic glass due to its greater contact angle of 109° compared with 7° for the hydrophilic glass as shown in Fig. 4 *A*–*C*. Also, the rate of evaporation against the hydrophilic glass is considerably more rapid than that for the hydrophobic glass.

The accumulation of moisture in the furrows due to occlusion is illustrated in Fig. 5. The optical images (Fig. 5 *A* and *B*) suggest that they become quite saturated at long times. However, the IR-OCT results (Fig. 5 *C* and *D*) show that the major fraction of the moisture is retained at the base of a furrow as it increases with time (Fig. 1*F*). The cross-sectional image of the moisture in a furrow after 180 s (Fig. 5*D*) resembles that after a similar time period for the wet case (Fig. 2*D*) and in both cases the side menisci are absent.

Discussion

Moisture Regulation. As mentioned previously, a wet finger pad in contact with glass is analogous to an array of microfluidic channels in which moisture is trapped by capillarity in the furrows. The contacts between the ridges and the counter surface result in the formation of sharp corners, as shown schematically in Fig. 4*D*, where side menisci have formed after the moisture has evaporated leaving a residual bulk meniscus. Although evaporation near the meniscus of such a system involves complex physics related to coupling between the hydrodynamics and mass transfer in the vapor phase, the phenomenon itself is well known (22–24). Compared with a circular cross-section capillary tube, for example, it has been shown that the side menisci greatly accelerate the evaporation rate by several orders of magnitude in a way that is independent of the relative humidity (22). The side menisci are pinned in the corners and provide a low-resistance pathway for water to evaporate near the entrance of the channel. Essentially, the analogy has been made that the side menisci siphon water to the entrance where it evaporates. Thus, as the bulk meniscus recedes inside a furrow due to evaporation at the water–air interface (Fig. 2 *A* and *B*), the corner films (side menisci) provide flow pathways for the water between the receding bulk meniscus and the furrow opening, as shown in *SI Appendix*, Fig. S7. The retreat of the bulk meniscus corresponds to a mean evaporation rate of ∼0.2 mm/s (Fig. 2*G*); it is slower for hydrophobic glass due to the greater contact angle (Fig. 4*A*). Further evaporation from the side menisci exhibits a much slower rate, corresponding to the disappearance of the side menisci. The ability to regulate hydration by evaporation through the furrows is important since there is strong evidence that excessive levels lead to a reduction in the friction (6, 15). This is indicative of a decrease in the interfacial shear stress when the contact area has reached an upper limit. That is, initially the increase in the contact area due to plasticization dominates by increasing the friction but, when apparently fully plasticized, the interfacial shear strength continues to decrease. This could arise because the interfacial shear strength is determined by interactions close to the interface while the change in contact area is a subsurface phenomenon.

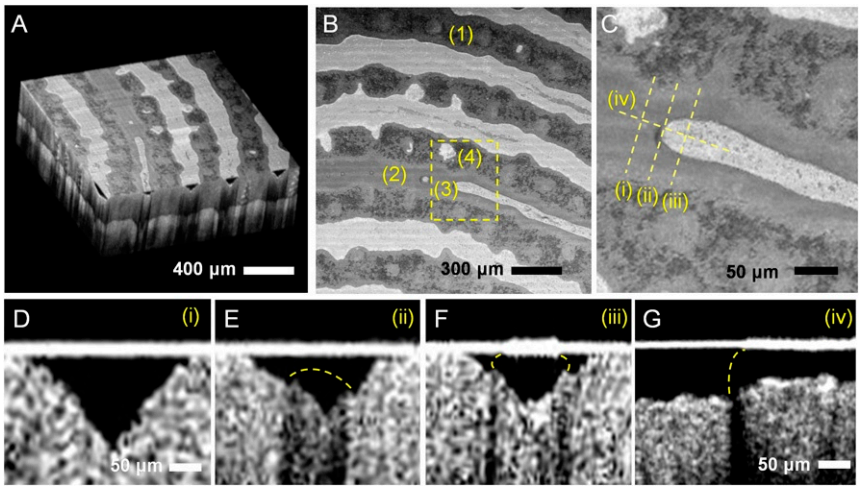

Fig. 3. IR-OCT tomographic images of a wet finger pad after 20 s. (*A*–*C*) Observation of menisci (bulk and side) formation in a wet furrow (*1*) after 20 s at increasing magnifications. Light gray regions are air gaps, darker regions of near-uniform gray level are moisture, and the darkest gray regions within fingerprint ridge boundaries are areas of localized skin–glass contact from which liquid is excluded. Liquid water (*2*) is visible between one pair of ridges and a bulk meniscus is present in contact with air (*3*). Sweat pores are approximately circular; some (*4*) are visible as white air voids while others with moisture appear darker gray. (*D*–*G*) Cross-sectional images as labeled in *C*. A side meniscus is observed in *F* (*SI Appendix*, Fig. S6). The air–water interface (yellow dashed lines) can be estimated from IR scattering on the glass surface and the optical path length difference corresponding to a step change in the height of the furrow. A receding bulk meniscus formed at the bulk water–air interface is observed in *G*.

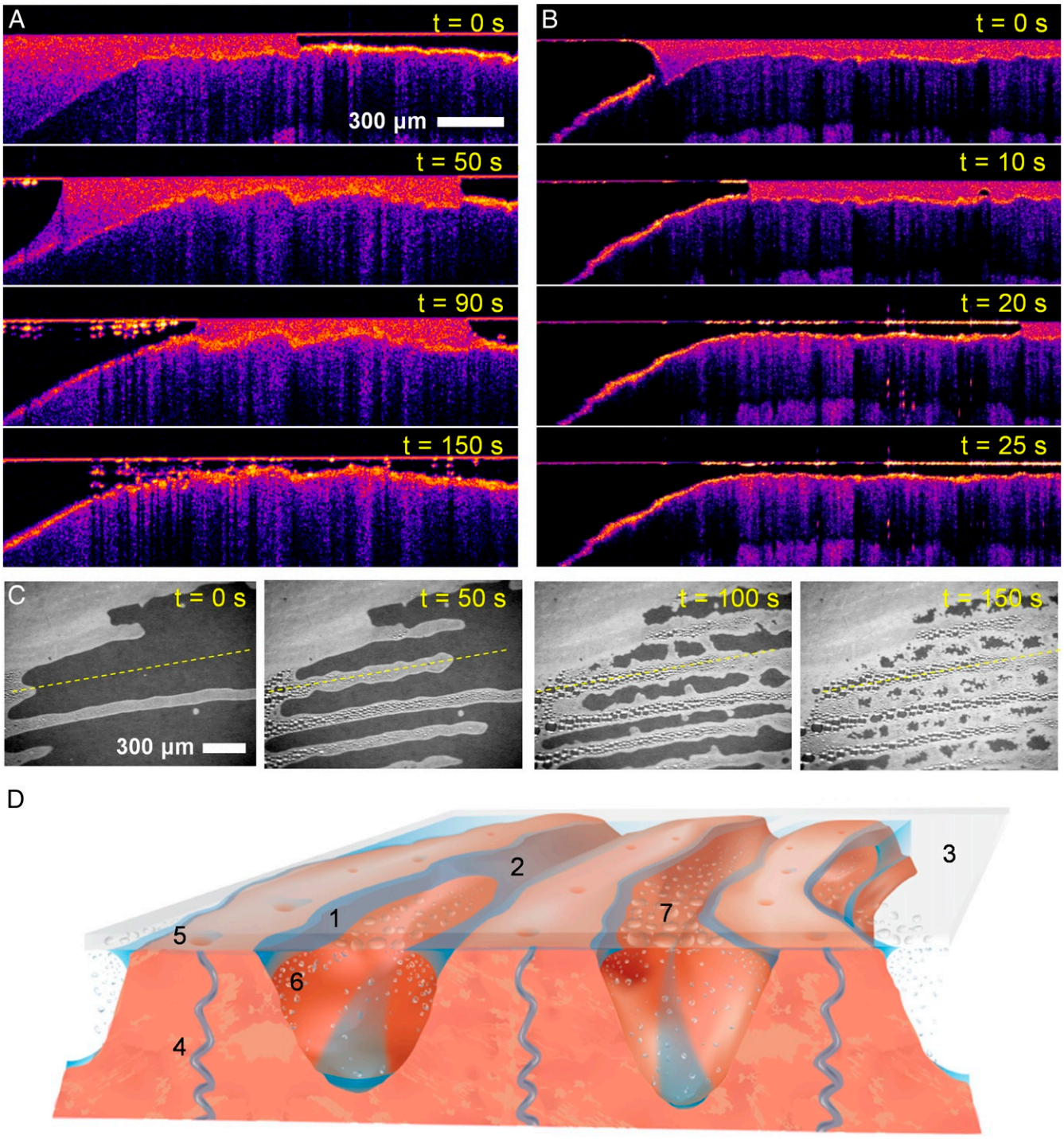

Fig. 4. (*A* and *B*) IR-OCT images of evaporation from a meniscus rendered more visible using fluorescent nanoparticles and hydrophobic and hydrophilic glass, respectively. The images are cut through the central region of a furrow, which for *A* corresponds to the dashed yellow lines in *C*. Condensed water droplets are visible at longer times after the moisture has evaporated only when hydrophobic glass is used due to the greater contact angle. Evaporation is slower for hydrophobic compared with hydrophilic glass since wicking at the moisture–vapor interface is retarded. (*C*) Optical images of the evaporation of a small water droplet compressed in a hydrophobic glass contact. The light regions within the contact boundary of the finger pad with the glass indicate air gaps; i.e., the skin is not in contact with the glass. The initially dark connected regions are space-filling liquid water. (*D*) Schematic diagram of the moisture regulation mechanism via bulk and side menisci induced evaporation in ridged skin showing a side meniscus (*1*), bulk meniscus (*2*), glass (*3*), sweat duct (*4*), sweat pore (*5*), evaporated moisture (*6*), and moisture condensing on the glass (*7*). All of the measurements involved the same participant.

In summary, the furrows have the function of a moisture-regulating mechanism, which ensures an optimal hydration of the keratin layer of the skin for maximizing the friction and reducing the probability of catastrophic slip. They appear to have the dual function of enhancing the evaporation of excess moisture but providing a moisture reservoir at their bases. For the initially

wet case, it is clear that at relatively short times the side menisci play a critical role in enhancing the evaporation rate. However, side menisci were not observed for both the wet case at relatively long times and the occluded state. Fig 1 *D* and *F* shows IR-OCT images in the fully occluded state and it is clear that the ridges conform closely to the counter surface such that it is reasonable to assume that the sweat pores are effectively blocked to the extent that further sweat secretion is inhibited. This is also the case for the wet state as exemplified by Fig. 3 *A*–*C*. Initially, the pores will be unblocked but as the ridges become plasticized a more intimate contact is formed, which corresponds to an increase in the friction, until there a cessation of the sweat secretion and a steady-state hydration level and friction are achieved. The ridges have a much smaller radius of curvature than that of the finger pad (see below) and thus, for a given normal force, the contact pressure will be greater than for flat skin, which will favor the blocking of the sweat pores. In the occluded state, the volume fraction of moisture increases only from ∼0.25 to ∼0.35 but it corresponds to a relatively large increase in the friction (Fig. 1 *G* and *H*). The Corneometer measures a mean value over a depth of 20 μm and, on the basis of Fig. 5*G*, it senses the quantity in the ridges since moisture is absent in the furrows at this depth. However, confocal Raman spectroscopy has shown that there is a much greater increase in the moisture near the surface of the skin that governs the skin since initially it is much less hydrated at the surface (25).

Implications for Finger Pad Friction. A finger pad in the dry state obeys Amontons' laws of friction; i.e., the friction is proportional to the applied normal force and independent of the gross area of contact (26). It is important to distinguish the gross contact area from the real value as defined by regions of intermolecular contact. The presence of the furrows will cause a reduction in the real contact area. However, it is because the surfaces of the ridges are topographically rough that Amontons' law is obeyed since the real contact area for such surfaces is proportional to the normal force (see *SI Appendix* for details). Moisture plasticizes the stratum corneum and it results in the topographic features, which are termed asperities, becoming more deformable due to a transition from a near-glassy to a rubbery state (27). Unlike dry ridged skin, which obeys Amontons' law, the coefficient of friction in the rubbery state depends on the contact area, which is consistent with the approximate increase in friction as the sizes of the finger pads increase (*SI Appendix*, Fig. S8). For a rough spherically capped elastic body in contact with a smooth rigid surface, the criterion for whether the asperities become flattened depends on the following parameter, κ, being <0.05 (28):

$$\kappa = \sigma_S \left(\frac{16 R E^{*2}}{9 W^2} \right)^{1/3}, \qquad [2]$$

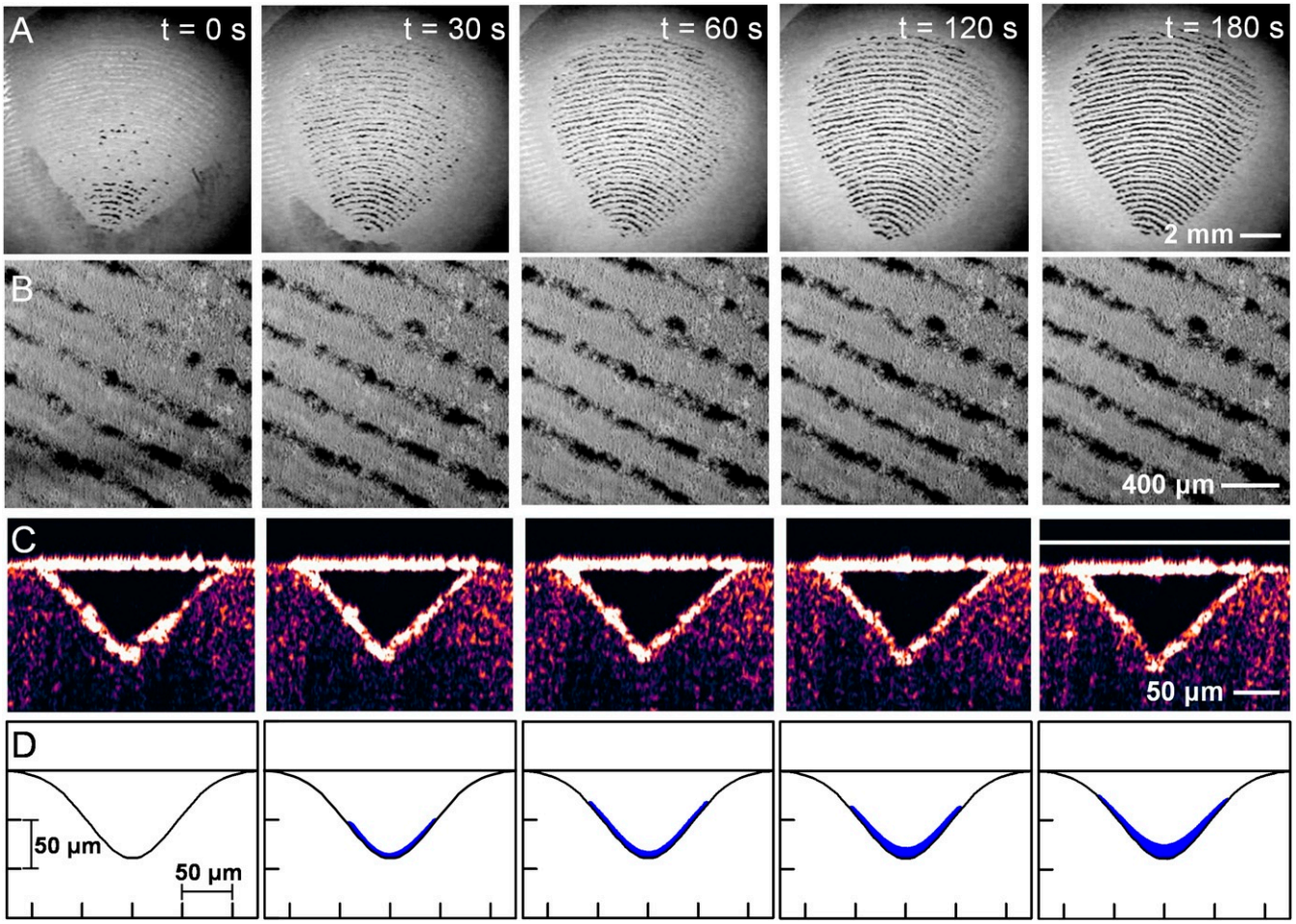

Fig. 5. The accumulation of moisture in the furrows between the epidermal ridges due to occlusion for an initially dry finger pad in contact with glass as a function of time. (*A*) Optical images. (*B*) Enlarged regions of *A*. (*C*) IR-OCT cross-sectional images of a typical furrow. (*D*) Cross-sections of the moisture distribution calculated from *C*.

where σ_S is the standard deviation in the distribution of asperity heights, R is the effective radius of the deformable body, and $E^* = E/(1-\nu^2)$ such that E and ν are the Young's modulus and Poisson's ratio. That is, for sufficiently small values of E^* and large values of W, the contact area is identical to that as if the body were smooth, which is typically found for elastomers. The model assumes that the body is homogeneous, but in the case of the epidermal ridges, plasticization by moisture reduces the value of E by many orders of magnitude to ~100 kPa (28), which is comparable to that of the bulk finger pad of ~35 kPa (29). Thus, in the plasticized state, for the current applied load of 0.48 N, a typical mean radius of curvature of a finger pad (15 mm), and a Poisson's ratio of 0.3, the expression is satisfied provided that σ_S <50 μm for the asperities on the surfaces of the ridges. This is much greater than would be expected given that a typical ridge height is ~80 μm (29). Moreover, it is a lower bound since the cylindrical radius of curvature of an epidermal ridge is ~0.3 mm, which will considerably decrease the value of κ due the greater contact pressure. It should be emphasized that the true contact area may be estimated only from the unloaded surface topography, for example by self-similar, randomly rough contact mechanics, which has been applied to flat skin (30). It involves complex numerical schemes but they are not essential here given that the critical value of σ_S for asperity flattening is much greater than what could be reasonably expected for the surfaces of the ridges (29).

Catastrophic Slip. In any grip event, a normal force is applied such that there is sufficient friction to eliminate slip. A particular advantage of the rubbery state is that the friction increases with the slip velocity within a limited range (12), which provides a self-arresting mechanism against an incipient slip. However, catastrophic slip could be caused by the formation of a water film between the ridges and the contact surface when a droplet of water is inserted (Fig. 2*B*). The interaction of the ridges with a surface is complex and has been observed to involve unconnected regions gradually coming into contact due to plasticization (27). Such regions initially involve an array of microcontacts that allow the ridges to retain moisture on their upper surfaces due to capillary action. Some of the moisture is absorbed into the ridges and the reduction in their stiffness causes the moisture to be squeezed into the furrows as they conform to the glass due to the action of the normal force and plasticization. This prevents a water film being formed that would result in a very low coefficient of friction (0.0015) as calculated for a smooth finger pad for a sliding velocity of 19 mm/s and a normal load of 11.7 N (6). The central film thickness, h_c was calculated to be 0.1 μm. This lubrication regime is known as "isoviscous elastohydrodynamic lubrication (IEHL)." The term isoviscous is used since the contact pressures are insufficient to increase the viscosity of the lubricant and "elastohydrodynamic" refers to the coupling of the elastic deformation of the contact due to the pressure generated by the flow of the lubricant. When there is solid–solid contact, it is referred to as the boundary regime. There is a transition between the two regimes, known as "mixed lubrication," in which the coefficient of friction reduces from of order 1 to values <0.01.

The criterion for the transition from the mixed to the IEHL regimes corresponds to the parameter Λ being in the range 5 to 10 and being <1 for the boundary regime (31). The value of Λ depends on the roughness of the bodies in contact and may be written in the form

$$\Lambda = \frac{h_c}{(\sigma_{ridges}^2 + \sigma_{glass}^2)^{1/2}}, \qquad [3]$$

where σ_{ridges} and σ_{glass} refer to the rms roughness of the ridges and counter surface, respectively. Assuming that $\sigma_{surface}$ = 0 μm and σ_{ridges} = 80 μm, and the normal force is the current value of 0.48 N, corresponding to h_c = 0.2 μm, then Λ = 0.002, which more than satisfies the condition that a fluid film would not be formed under these conditions. This also corresponds to the coefficients of friction being >1. Eq. **3** does not account for any deformation of the ridges but this requires complex numerical analysis, e.g., ref. 32. Nevertheless, it has been shown that it is a close approximation for rough elastomers (33) and since $\Lambda \ll 1$, it is reasonable to conclude that a fluid water film is not formed at a sliding speed of 19 mm/s, which is comparable to that applied during tactile events.

Implications for Natural Surfaces. The current work was necessarily restricted to glass as a counter surface given the requirement of optical transparency. However, natural surfaces may be rough and permeable to moisture. Materials such as paper absorbed any secreted sweat and the friction decreases with increasing contact time (12). Thus, the relative timescales of moisture accumulation and counter surface permeation is a critical parameter. As described above, in the near glassy state, the friction is independent of the gross contact area and is reduced when in contact with a rough surface. However, the plasticization of the ridges will allow them to more easily conform to surface topographical features and thus increase the friction by an interlocking mechanism. There is clear evidence that this is the case since the friction of wet finger pads on rough glass (R_a ~ 45 μm) is considerably greater than that for smooth glass and the difference increases with increasing contact pressure (8). However, in the case of a dry contact, the friction against rough glass is less than that for the smooth glass as would be expected for a multiple-asperity contact (8).

When interlocking occurs, the component of the applied frictional force acting in the sliding direction on an asperity increases the local value of the normal force. Thus the frictional force, F_{int}, may be written in the following form (34):

$$F_{int} = \begin{cases} W\tan(\lambda) + F_{adh}\sec(\lambda), & \text{if } F_{adh} > 0. \\ 0, & \text{if } F_{adh} = 0, \end{cases} \qquad [4]$$

where λ is the angle of inclination of the asperity and F_{adh} is the adhesion component of friction corresponding to a smooth planar counter surface. The first term on the right-hand side represents the force to slide over an asperity so that when $\lambda = 0$, Eq. **4** reduces to the smooth case. When $F_{adh} = 0$, it reduces to the Euler relationship but then $F_{int} = 0$ since sliding over an asperity without interfacial friction does not dissipate energy but this was not understood by the early workers in the field such as Euler and Coulomb. The second term is the adhesive component augmented by the increase in the local normal force, which represents the energy dissipated per unit sliding distance. It is possible to readily perceive such interlocking by rubbing a hair fiber between the thumb and index finger since the friction is greater toward than away from the scalp due to the sharp edges of the sawtooth geometry of the hair cuticles that catch on the ridges, which have a height of about 500 nm. It is a testament to our tactile abilities that we can perceive a topographical feature that is ~10 nm (35), which represents a greater spatial resolution than that of vision.

Conclusion

Since, in repeated grip experiments, the moisture level of the finger pad keratin increased or decreased in such a way that created a maximum in the friction, it has been proposed that finger pads exhibit moisture regulation (15). The current data provide direct evidence of the underlying moisture regulation mechanism that, for the wet case, the furrows act as microfluidic channels

in which the bulk and the side menisci promote evaporation of excess water but with sufficient retained moisture that the ridges remain in a plasticized state. However, at long times, the side menisci were not observed as was the case for initially dry finger pads. It is believed that the greater contact pressure arising for ridged compared with flat skin has the dual function of the blocking of the sweat pores and inhibiting hydrodynamic lubrication that would lead to catastrophic slip. Thus, we have discovered direct evidence that explains the high density of sweat glands in the fingerprint ridges and their recruitment under conditions of high psychological stress rather than thermoregulation. Due to experimental constraints, the work was carried out using optically flat glass as the counter surface. We believe that the findings are applicable to natural surfaces that may be topographically rough, provided that the rate of moisture absorption is less than that of moisture accumulation.

In a wider context, the understanding of the influence of finger pad friction in the partially or fully occluded state will contribute to the development of more realistic tactile sensors, e.g., for applications in robotics and prosthetics, and also haptic feedback systems, e.g., for touch screens and virtual reality environments. For example, ultrasonic lubrication is commonly employed in haptic displays but the effectiveness is reduced for dry compared with moist finger pads (36). For fine-textured surfaces such as textiles, tactile discrimination relies on lateral vibrations (37). If such vibrations are recorded and applied to a finger pad, the discriminative performance of subjects is remarkably effective but the absence of sliding friction prevents a realistic perception of the actual texture (38). This work demonstrates the profound influence of friction in the way that we perceive the tactile attributes of an object.

Materials and Methods

Participants. Six males in the age range 27 to 33 y participated in the measurements. All of the data presented in the main text are for a single participant to compare the data obtained from MHz, THz, IR, and visible light. Additional data for another participant are added in *SI Appendix*, Fig. S5 *A* and *B*. For the other four participants, the hydration measurements (*SI Appendix*, Fig. S5*C*) were made to establish that the hydration behavior is consistent albeit with some variation from person to person. The hydration and friction measurements for each participant were repeated more than three times to calculate the mean and error bars as ± 1 SD. Every participant gave informed consent to participate in the experiments. The study was approved by Seoul National University Institutional Review Board (IRB no. 1905/002-003).

Protocol for the Dry and Wet States. Initially, the participants washed their hands using water and soap, and they were environmentally equilibrated for 10 min in a controlled room at 23.5 ± 0.5 °C and $40 \pm 2\%$ relative humidity (RH). In the dry state, a lint-free tissue was used to remove any surface moisture secreted by sweating. For the wet state, 1.0 μL of water was applied between the plate and fingertip using a micropipette.

Friction Measurements. The friction of a fingertip was measured using a tribometer with a horizontal motor-driven translation stage equipped with two-axis transducers each having a resolution of 33 mN. A photographic image of the tribometer is shown in *SI Appendix*, Fig. S1. The tangential transducer (CZL639HD; Phidgets Inc.) had a force range of 0 to 1 N and the normal transducer (CZL616 C; Phidgets Inc.) had a force range of 0 to 7.65 N. An optical glass plate (76 × 26 mm; Marienfeld), which had been cleaned by a dry wiper (KIMTECH science wiper), was attached to the motion stage and a subject applied a normal force of 0.48 ± 0.04 N to the glass by pressing the selected finger. The stage was set to a reciprocating motion with a speed of 2.5 mm/s and a displacement of 8 mm for 300 s. During this period both the tangential and normal forces were monitored. The coefficient of friction was calculated as the ratio of the maximum static friction force just before the finger slip occurs and the normal force measured instantaneously with the maximum static friction.

Hydration Level Measurement (MHz Frequency). To measure the hydration of a fingertip, a Corneometer (CM 825; Courage + Khazaka Electronic GmbH) was employed (*SI Appendix*, Fig. S2). The probe measures capacitance and consists of an interdigitated electrode pattern that creates a surface field near the probe that responds to the moisture content. The Corneometer detects the charge time and displays the hydration level of the skin as a value from 0 to 120 (arbitrary units), with calibration being done using cellulose filter paper. The value is linearly dependent on the applied amount of water (39). To determine the penetration depth, supplementary experiments were performed on a cellulose filter pad with a polyurethane film of thickness 15 μm inserted between the pad and the probe. Since the polyurethane film is transparent to the device, increasing the number of films corresponds to increasing the distance between the probe and the sample. An exponential decay of the hydration level with the distance between the probe and sample was measured. A 90% decrease in the hydration level represents a sensor penetration depth of approximately 20 μm (*SI Appendix*, Fig. S9). The hydration level (arbitrary units) is calibrated with the dielectric constant of the sample (40). We fitted the hydration level–dielectric constant relationship with an exponential expression ($R^2 = 0.90$). We also correlated the dielectric constant with the volume fraction of water using the effective medium theory, which provides a correlation between the hydration level and the volume fraction of water (41) (*SI Appendix*, Fig. S9).

Imaging Methods (Infrared and Visible Light). The moisture hydrodynamics involving a fingerprint against a glass plate were quantified by direct visualization using OCT (GAN320C1; Thorlabs Inc.) and a CCD camera (ICS; Sometech Inc.). IR waves with a wavelength of 1,300 nm were used, which produces a tomographic image (42). It allowed the formation of side and bulk menisci and also the evaporated moisture droplets on the glass to be imaged with the profile of the water meniscus obtained from the path length of the reflected IR beam in the furrows of fingerprint ridges. The subsequent moisture evaporation in the furrows was visualized with the aid of a 1% vol/vol dispersion of 500-nm fluorescent nanoparticles (G500; Thermo Fisher Scientific). The evaporation rate was also measured by visible light using a CCD camera. To acquire contact information of the finger pad with the glass, the CCD camera was employed using visible light (halogen lamp). The intensity of the visible light reflected at the interface of the glass was imaged. The position of the bulk meniscus by space-filling liquid water was obtained from the dark region in the image. The displacement of the meniscus as a function of time due to evaporation was estimated from the rate of disappearance of the dark region. The condensed water on the surface of the glass due to moisture evaporation was directly visualized using both IR waves and visible light (Fig. 4).

Terahertz Spectral Response of Ridge Skin. An additional measurement of the profile of the moisture in the furrows was made using a polarization-tunable THz-TDS system (TAS7500SP; Advantest Corporation). A THz free-standing wire grid polarizer (G30x10-L; Microtech Instruments, Inc.) was employed to adjust the direction of polarization of the incident THz waves to the skin (*SI Appendix*, Fig. S3). When a femtosecond laser is irradiated onto a linear dipole-shaped metal pattern (photoconductive antenna) on a low temperature grown gallium arsenide (LT-GaAs) substrate, a pulse with a strong linear polarization of a broadband (0.1 to 3 THz) frequency is generated. This pulse changes the polarization between $-45°$ and $+45°$ through two polarizers (*SI Appendix*, Fig. S3). Then, the polarized THz pulse is reflected from the sample and enters the detector. Since the detection part also uses a linear dipole antenna on the LT-GaAs substrate, it is sensitive to only one component of the electric field. This reflected time domain signal is converted to the frequency domain by fast Fourier transform (FFT). It was observed that a strong resonance occurs when the direction of polarization is parallel to the fingerprint texture and disappears when it is perpendicular. The validity of the data was confirmed by ensuring that the resonances were greater than the noise level of the THz-TDS system (43). The response was modeled using finite-difference time domain software (44) (*SI Appendix*, Fig. S10) and shown to be sensitive to moisture at 5 GHz per 1 μm in height (*SI Appendix*, Fig. S11). The simulated response to THz waves for a dry finger pad agrees reasonably with that measured (*SI Appendix*, Fig. S12). The principle of Fabry–Perot resonance is shown schematically in *SI Appendix*, Fig. S13.

Data Availability. All data discussed in this paper are available at Figshare, https://doi.org/10.6084/m9.figshare.13139489.v1 (45).

ACKNOWLEDGMENTS. This work was funded by the National Research Foundation of Korea through the Korea government Ministry of Science and Information Communication and Telecommunication (MSIT) under Grants 2016R1A3B1908336 and 2018M3A7B4070990.

1. M. Wiertlewski, R. F. Friesen, J. E. Colgate, Partial squeeze film levitation modulates fingertip friction. *Proc. Natl. Acad. Sci. U.S.A.* **113**, 9210–9215 (2016).
2. P. Weiner, C. Neef, Y. Shibata, Y. Nakamura, T. Asfour, An embedded, multi-modal sensor system for scalable robotic and prosthetic hand fingers. *Sensors* **20**, 101 (2019).
3. M. Cartmill, The volar skin of primates: Its frictional characteristics and their functional significance. *Am. J. Phys. Anthropol.* **50**, 497–509 (1979).
4. M. W. Hamrick, Functional and adaptive significance of primate pads and claws: Evidence from new world anthropoids. *Am. J. Phys. Anthropol.* **106**, 113–127 (1998).
5. R. Lewis, M. Carré, S. Tomlinson, Skin friction at the interface between hands and sports equipment. *Procedia Eng.* **72**, 611–617 (2014).
6. S. Tomlinson, R. Lewis, X. Liu, C. Texier, M. Carré, Understanding the friction mechanisms between the human finger and flat contacting surfaces in moist conditions. *Tribol. Lett.* **41**, 283–294 (2011).
7. G. Chimata, C. J. Schwartz, Investigation of the effect of the normal load on the incidence of friction blisters in a skin-simulant model. *Proc. IME J. J. Eng. Tribol.* **229**, 266–272 (2015).
8. S. Derler, L. C. Gerhardt, A. Lenz, E. Bertaux, M. Hadad, Friction of human skin against smooth and rough glass as a function of the contact pressure. *Tribol. Int.* **42**, 1565–1574 (2009).
9. K. Wertheim, A. Maceo, The critical stage of friction ridge and pattern formation. *J. Forensic Ident.* **52**, 35–85 (2002).
10. S. Adelman, C. R. Taylor, N. C. Heglund, Sweating on paws and palms: What is its function? *Am. J. Physiol. Content* **229**, 1400–1402 (1975).
11. P. H. Warman, A. R. Ennos, Fingerprints are unlikely to increase the friction of primate fingerpads. *J. Exp. Biol.* **212**, 2016–2022 (2009).
12. M. J. Adams *et al.*, Finger pad friction and its role in grip and touch. *J. R. Soc. Interf.* **10**, 20120467 (2013).
13. N. A. Taylor, C. A. Machado-Moreira, Regional variations in transepidermal water loss, eccrine sweat gland density, sweat secretion rates and electrolyte composition in resting and exercising humans. *Extreme Physiol. Med.* **2**, 4 (2013).
14. S. M. Pasumarty, S. A. Johnson, S. A. Watson, M. J. Adams, Friction of the human finger pad: Influence of moisture, occlusion and velocity. *Tribol. Lett.* **44**, 117–137 (2011).
15. T. André, P. Lefèvre, J. L. Thonnard, Fingertip moisture is optimally modulated during object manipulation. *J. Neurophysiol.* **103**, 402–408 (2009).
16. R. K. Sivamani, J. Goodman, N. V. Gitis, H. I. Maibach, Coefficient of friction: Tribological studies in man–an overview. *Skin Res. Technol.* **9**, 227–234 (2003).
17. N. Gitis, R. Sivamani, Tribometrology of skin. *Tribol. Trans.* **47**, 461–469 (2004).
18. S. Tomlinson, R. Lewis, M. Carré, Review of the frictional properties of finger-object contact when gripping. *Proc. IME J. J. Eng. Tribol.* **221**, 841–850 (2007).
19. S. Derler, L. C. Gerhardt, Tribology of skin: Review and analysis of experimental results for the friction coefficient of human skin. *Tribol. Lett.* **45**, 1–27 (2012).
20. J. van Kuilenburg, M. A. Masen, E. van der Heide, A review of fingerpad contact mechanics and friction and how this affects tactile perception. *Proc. IME J. J. Eng. Tribol.* **229**, 243–258 (2015).
21. A. D. Dussaud, P. M. Adler, A. Lips, Liquid transport in the networked microchannels of the skin surface. *Langmuir* **19**, 7341–7345 (2003).
22. F. Chauvet, P. Duru, S. Geoffroy, M. Prat, Three periods of drying of a single square capillary tube. *Phys. Rev. Lett.* **103**, 124502 (2009).
23. J. C. T. Eijkel *et al.*, Strongly accelerated and humidity-independent drying of nanochannels induced by sharp corners. *Phys. Rev. Lett.* **95**, 256107 (2005).
24. F. Doumenc, B. Guerrier, Drying of a solution in a meniscus: A model coupling the liquid and the gas phases. *Langmuir* **26**, 13959–13967 (2010).
25. A. K. Dąbrowska *et al.*, In vivo confirmation of hydration-induced changes in human-skin thickness, roughness and interaction with the environment. *Biointerphases* **11**, 031015 (2016).
26. B. M. Dzidek *et al.*, "Role of occlusion in non-Coulombic slip of the finger pad" in *Haptics: Neuroscience, Devices, Modeling, and Applications*, M. Auvray, C. Duriez, Eds. (Springer Berlin Heidelberg, Berlin, Heidelberg, Germany, 2014), pp. 109–116.
27. B. Dzidek, S. Bochereau, S. A. Johnson, V. Hayward, M. J. Adams, Why pens have rubbery grips. *Proc. Natl. Acad. Sci. U.S.A.* **114**, 10864 (2017).
28. K. L. Johnson, *Contact Mechanics* (Cambridge University Press, 1987).
29. B. M. Dzidek, M. J. Adams, J. W. Andrews, Z. Zhang, S. A. Johnson, Contact mechanics of the human finger pad under compressive loads. *J. R. Soc. Interf.* **14**, 20160935 (2017).
30. A. E. Kovalev, K. Dening, B. N. J. Persson, S. N. Gorb, Surface topography and contact mechanics of dry and wet human skin. *Beilstein J. Nanotechnol.* **5**, 1341–1348 (2014).
31. B. J. Hamrock, S. R. Schmid, B. O. Jacobson, *Fundamentals of Fluid Film Lubrication* (CRC Press, 2004).
32. B. N. J. Persson, M. Scaraggi On the transition from boundary lubrication to hydrodynamic lubrication in soft contacts. *J. Phys. Condens. Matter* **21**, 185002 (2009).
33. J. de Vicente, J. Stokes, H. Spikes, The frictional properties of Newtonian fluids in rolling–sliding soft-ehl contact. *Tribol. Lett.* **20**, 273–286 (2005).
34. M. J. Adams, B. J. Briscoe, T. K. Wee, The differential friction effect of keratin fibres. *J. Phys. Appl. Phys.* **23**, 406–414 (1990).
35. L. Skedung *et al.*, Feeling small: Exploring the tactile perception limits. *Sci. Rep.* **3**, 2617 (2013).
36. D. Gueorguiev, E. Vezzoli, A. Mouraux, B. Lemaire-Semail, J. L. Thonnard, The tactile perception of transient changes in friction. *J. R. Soc. Interf.* **14**, 20170641 (2017).
37. B. Khojasteh, M. Janko, Y. Visell, Complexity, rate, and scale in sliding friction dynamics between a finger and textured surface. *Sci. Rep.* **8**, 13710 (2018).
38. M. Wiertlewski, J. Lozada, V. Hayward, The spatial spectrum of tangential skin displacement can encode tactual texture. *IEEE Trans. Robotics* **27**, 461–472 (2011).
39. J. W. Fluhr *et al.*, Comparative study of five instruments measuring stratum corneum hydration (Corneometer CM 820 and CM 825, Skicon 200, Nova DPM 9003, DermaLab). Part I. In vitro. *Skin Res. Technol.* **5**, 161–170 (1999).
40. A. O. Barel, P. Clarys, In vitro calibration of the capacitance method (Corneometer CM 825) and conductance method (Skicon-200) for the evaluation of the hydration state of the skin. *Skin Res. Technol.* **3**, 107–113 (1997).
41. S. Berthier, J. Lafait, Effective medium theory: Mathematical determination of the physical solution for the dielectric constant. *Optic Commun.* **33**, 303–306 (1980).
42. G. J. Tearney *et al.*, In vivo endoscopic optical biopsy with optical coherence tomography. *Science* **276**, 2037–2039 (1997).
43. R. M. Woodward *et al.*, Terahertz pulse imaging in reflection geometry of human skin cancer and skin tissue. *Phys. Med. Biol.* **47**, 3853–3863 (2002).
44. T. Weiland, Time domain electromagnetic field computation with finite difference methods. *Int. J. Numer. Model. Electron. Network. Dev. Field.* **9**, 295–319 (1996).
45. S.-M. Yum, Dataset for the article "Fingerprint ridges allow primates to regulate grip". Figshare. https:/doi.org/10.6084/m9.figshare.13139489.v1. Deposited 11 November 2020.